

A general and modular approach to solid-state integration and readout of zero-dimensional quantum systems

Authors:

Marzieh Kavand^{1,6}, Zoe Phillips^{1†}, William H. Koll^{1†}, Morgan Hamilton^{1†}, Ethel Perez-Hoyos¹, Rianna Greer², Ferdous Ara¹, Dan Pharis¹, Kian Maleki³, Mingyu Xu⁴, Takashi Taniguchi⁵, Paul Canfield⁴, Michael E. Flatté^{3,7}, Danna E. Freedman², Jay Gupta¹, Ezekiel Johnston-Halperin^{1*}

Affiliations:

¹Department of Physics, The Ohio State University, Columbus, Ohio 43210, USA.

²Department of Chemistry, Massachusetts Institute of Technology, Cambridge, Massachusetts 02139, USA.

³Department of Physics and Astronomy, University of Iowa, Iowa City, Iowa, USA.

⁴Ames National Laboratory and Department of Physics and Astronomy, Iowa State University, Ames, Iowa, 50010, USA.

⁵International Center for Materials Nanoarchitectonics (MANA), National Institute for Materials Science, 1-1 Namiki Tsukuba Ibaraki 305-0044, Japan.

⁶Department of Physics and Astronomy, The University of Alabama, Tuscaloosa, Alabama, 35487, USA.

⁷Department of Applied Physics and Science Education, Eindhoven University of Technology, 6500 MB Eindhoven, The Netherlands

[†]These authors contributed equally to this work.

*Correspondence to: johnston-halperin.1@osu.edu

Electronic spectroscopy of zero-dimensional (0D) quantum systems, including point defects in solids^{1–3}, atomic states^{4,5}, and small molecules^{6–8}, is a critical tool for developing a fundamental understanding of these systems, with applications ranging from solid-state⁹ and molecular^{10,11} materials development to emerging technologies rooted in quantum information science¹². Toward this end, scanning tunneling spectroscopy (STS) has demonstrated atomic-scale sensitivity, but is not easily scalable for applications, whereas device-based approaches rely on embedding these systems within a solid-state tunnel junction (TJ) and are not generally applicable. Here we demonstrate an all-electrical readout mechanism for these quasi-0D states that is modular and general, dramatically expanding the phase space of accessible quantum systems and providing an approach that is amenable to scaling and integration with other solid-state quantum technologies. Our approach relies on the creation of high-quality tunnel junctions via the mechanical exfoliation and stacking of multi-layer graphene (MLG) and hexagonal boron nitride (hBN) to encapsulate the target quantum system (QS) in an MLG/hBN/QS/hBN/MLG heterostructure. This structure allows for electronic spectroscopy and readout of candidate quantum systems through a combination of Coulomb^{13–15} and spin-blockade^{16,17}, providing access to entire classes of quantum systems that have previously only been accessible via optical spectroscopy or magnetic resonance measurements of large ensembles, if at all.

We demonstrate the power and modularity of this approach by the consideration of both intrinsic and encapsulated quantum systems in the form of point defects in hexagonal boron nitride (hBN) and the molecular qubit vanadyl phthalocyanine (VOPc), a spin 1/2 molecular qubit that has demonstrated long coherence times in an isostructural diamagnetic host (up to 1 μ s at room temperature⁸), respectively. The differential conductance (dI/dV) of these devices reveals the

underlying electronic structure, and in the case of VOPc devices, we confirm both qualitative and quantitative agreement with STS measurements and the theory of VOPc electronic structure¹⁸. These devices are fully compatible with existing solid-state quantum technologies (*e.g.*, silicon quantum dots¹⁹ and superconducting qubits²⁰) and experimental protocols^{21–23}, and our fabrication protocols are compatible with monolithic integration of microwave components. These results therefore demonstrate a modular and general approach to the investigation and manipulation of novel quantum systems that will allow for a more systematic approach to the design and manufacturing of new quantum technologies. For example, the motion of charge through a 0D structure involves, at least temporarily, an initial and/or final state that possesses spin; study of this transport, especially in small magnetic fields, has been used to reveal quantum-technology-relevant quantities such as low-temperature spin coherence times in individual quantum dots^{24,25}, and at room temperature the hyperfine fields and exchange interactions of small numbers of defects^{26–28}.

There are several key constraints to consider for the integration of quantum systems into a device architecture to ensure its efficacy: (i) the relevant quantum properties should be preserved in the integrated state, (ii) the electronic response of the integrated device should allow for readout of the relevant quantum properties, (iii) the quantum system should be protected from fabrication processes, (iv) the device architecture should be compatible with existing quantum technologies. Mechanical exfoliation and stacking of 2D materials provide a low-temperature and nonreactive approach to building modular tunnel junctions with the potential to satisfy these criteria. The mechanical nature of 2D exfoliation and stacking provides facile encapsulation of quantum systems between 2D layers, including molecules, adatoms, and quantum point defects (QPD), that avoids the high temperatures and reactive chemistries typically involved in traditional fabrication

processes. Further, exfoliation and stacking provide a facile route to the fabrication of high-quality tunnel junctions with atomically precise control of barrier thickness and strongly suppressed pinhole formation. Prior work in related tunnel junctions in the Coulomb blockade regime has demonstrated the potential for high-fidelity quantum readout^{16,29,30}. Finally, this approach leverages a large body of prior work in integrating 2D materials into existing quantum architectures such as on-chip microwave resonators³¹, transmons³², and spin qubits^{19,30}.

Fig. 1a shows a schematic illustration of one such hBN-based 2D tunnel junction (2D-TJ) device (see Supplementary Note S1 for a more detailed discussion) with graphitic contacts and gold electrodes. The active area of the device is stacked with mechanically exfoliated hBN and graphite using well-established dry transfer techniques³³, wherein the graphitic contacts consist of multilayer graphene (MLG) of typical thickness 6.5 ± 3.5 nm, well into the bulk graphitic regime. To achieve the desired tunneling conditions, the insulating hBN layer is selected to be between 1.5 nm and 3.5 nm, confirmed by atomic force microscopy (AFM) (see Extended Data Fig. 1a). The thickness of the hBN barrier dictates the current of the nonlinear tunneling response, ranging from tens of nanoamps to a few microamps in this regime. Gold electrodes are deposited onto completed stacks, with care taken to avoid extending the metal electrodes over the active area of the device in order to suppress metal migration and the creation of parasitic current pathways. Figure 1b shows an optical image of a representative 2D-TJ device with an hBN tunnel barrier of 3.01 ± 0.66 nm and an active area of $3.1 \mu\text{m}^2$.

Initial device characterization is performed at room temperature, as shown in Fig. 1c for a device constructed with hBN sourced commercially from HQ Graphene (thickness of 4 ± 0.5 nm). A schematic energy diagram is shown in the inset. The black curve shows the tunneling current

through the device while sweeping the bias voltage (I-V response), revealing a contribution from direct tunneling through the barrier and additional tunneling processes within the device (*e.g.*, the plateau at a source-drain bias of ± 0.30 V). To highlight these additional processes, synchronous measurement of dI/dV is performed using frequency modulation and homodyne detection with a lock-in amplifier, as represented by the purple curve in Fig. 1c. These data show both direct tunneling and broad peaks that appear at, for example, ± 0.30 V and ± 0.60 V, suggesting the presence of resonant tunneling processes through quantum states with energies lying within the bandgap of the hBN.

To resolve these resonances, additional measurements were performed at a temperature of 15 K (purple curve in Fig. 2a) for a similar device (hBN thickness of 3.01 ± 0.66 nm), and the reduction in thermal broadening reveals additional structure in the resonances that appear at ± 0.2 V and ± 0.50 V. The probability of direct tunneling depends on the thickness of the tunnel barrier and is suppressed exponentially with increasing tunnel barrier thickness (as shown in Extended Data Fig. 1b), so each peak in Fig. 2a (purple data) could in principle represent either elastic defect-assisted tunneling, inelastic phonon-assisted tunneling, or some combination of the two.

To further characterize these resonances, two additional sets of devices are investigated. The second set of devices is constructed using hBN synthesized³⁴ (see Supplementary Note S2) at Ames National Lab (blue curve; hBN thickness of 1.66 ± 0.33 nm and area of $4.72 \mu\text{m}^2$). While the relative amplitude of the tunneling resonances changes as compared to the commercially-supplied hBN, it is notable that the position (voltage) of many of the peaks reproduces, for example, the symmetric resonant peaks around ± 0.21 V and similar peaks around -0.55 V, -0.3 V, and $+0.73$ V. The third set of devices is constructed with ultra-pure hBN synthesized at the

International Center for Materials Nano Architectonics (MANA)³⁵ (green curve; hBN thickness of 2.01 ± 0.33 nm and area of $2.09 \mu\text{m}^2$). This material is known to yield devices with extremely high electron mobility when used to isolate, *e.g.*, single-layer graphene from its environment, suggesting an exceptionally low level of charge-active defects³⁶. This hypothesis is borne out by dI/dV measurements, which show strong suppression of resonant tunneling as compared to the first two devices (a single weak resonance is observed at -0.23 V, as shown in Extended Data Fig. 2).

These results confirm that the tunneling resonances observed in both commercial and Ames Lab synthesized hBN are due to intrinsic defects within the hBN material and not extrinsic impurities or contamination. As detailed in Supplementary Note S1, this stacking process ensures a clean hBN interface without chemical exposure. Moreover, during the annealing process, thermal changes are gradual to prevent structural and functional alterations in the 2D layers caused by thermal shock. The rich variety of predicted structural defects predicted for hBN makes a definitive assignment of these resonances to specific atomic structures difficult. For example, prior work in modeling defect formation in hBN predicts the formation of native defects such as vacancies, antisites, and interstitial structural defects during hBN growth, with the most energetically favorable being carbon, oxygen, and hydrogen impurities³⁷⁻³⁹. Further, each defect can in principle generate multiple peaks, for example, boron vacancies (V_B) have multiple different charge states: *e.g.*, neutral, -1, and -2, with C_{3v} symmetry for the neutral and -2 states and D_{3h} in the -1 state³⁹. Finally, the commercially supplied hBN is polycrystalline, potentially leading to varying orientations within the TJ for chemically identical defect states. However, the reproducibility across two different sets of materials synthesized in two different laboratories (commercial and Ames hBN) provides strong evidence that these resonances do in fact arise from

hBN defects. In addition, the absence of the peaks in the tunneling spectra from MANA hBN further supports the absence of impurities from residues deposited during our fabrication process or other extrinsic contamination.

These measurements indicate that hBN-TJs can provide a sensitive probe of the electronic structure of atomic defects in the tunnel barrier. To further test this proposition, additional hBN crystals are prepared at Ames lab wherein carbon has been introduced during hBN growth (see Supplementary Note S2). This excess carbon can contribute to the creation of substitutional and interstitial carbon defects as well as C-nucleated and C-catalyzed defects^{37,38,40}. Tunneling spectra from a device fabricated from this material are shown in Fig. 2b, where an additional constellation of extremely sharp tunneling resonances is revealed. These peaks are highly reproducible, both the main figure and the inset show trace/re-trace scans of dI/dV confirming these sharp features are stable and well-defined states. Further analysis shows that individual peaks show thermal broadening consistent with tunneling spectroscopy of atomic point defects (see Extended Data Fig. 3).

These results demonstrate the facility with which these 2D tunnel junctions can be used to measure detailed electronic tunneling spectra for quantum point defects and impurities within a solid-state host, suggesting that this architecture may be further generalized to include encapsulated quantum systems. Specifically, we consider the molecular spin qubit VOPc. ⁸Metallophthalocyanines are known molecular semiconductors, generally demonstrate environmental stability, and can be sublimed using standard evaporation techniques^{8,41} resulting in well-ordered films, making them attractive targets for device integration^{42,43}. To validate this potential for incorporation into the solid-state quantum devices described above, we first studied VOPc⁴⁴ (see Supplementary Note S3) thin films on a monolayer of hBN grown on highly-oriented pyrolytic graphite (HOPG) using scanning tunneling microscopy (STM). VOPc was deposited under ultra-high vacuum conditions

(~1E-9 mbar)⁴⁵, with a deposition rate of ~1 monolayer/min determined by STM imaging⁴⁶. Fig. 3a and 3b show the molecular structure of VOPc and a schematic representation of the STM geometry, illustrating the heterostructure formed by VOPc deposition on hBN/HOPG. Fig. 3c displays an STM topography image of a thin film of VOPc measured at 5 K, revealing the self-assembly of VOPc into a well-ordered film on the surface of the hBN/HOPG substrate whose orientation is consistent with the schematic in Fig. 3b. Consistent with the nominal deposition rate and prior STM studies⁴⁷, this image suggests the film comprises a uniform bilayer of VOPc⁴⁷, with a low density of defects such as molecular vacancies or 3rd layer molecules.

Differential conductance spectra taken at selected positions within the layer at a temperature of 5 K are shown in Fig. 3d. Clear peaks in the dI/dV are resolved, representing the HOMO, LUMO and excited states of the VOPc film⁴⁸ at these distinct locations, with a weak direct tunneling background evident at higher tip-sample bias. The energies of the peaks corresponding to resonant tunneling vary with tip position, revealing spatial variation in the molecular orbitals involved in the tunneling process as shown in the spectra in Fig. 3d. Furthermore, spatial variation is observed in STM images of bare hBN and dI/dV maps of the VOPc surface (refer to Extended Data Fig. 4). This suggests that other factors, including the moiré pattern of hBN/HOPG and local defects in both HOPG and hBN, could contribute to spatial variations in the local energy structure and density of states.

The STM images indicate that VOPc thin films should form high-quality barriers in hBN TJ devices. In order to test this prediction, VOPc heterostructures were assembled in a five-layer stack (MLG/hBN/VOPc/hBN/MLG; see Supplementary Note S4). This tunneling device was then characterized by both I-V and dI/dV measurements at a temperature of 15 K (Fig. 3e), as with the MLG/hBN/MLG structures in Fig. 2. The dI/dV response reveals a direct tunneling background

similar to the response of MLG/hBN/MLG devices fabricated from MANA hBN, but with the addition of tunneling resonances at voltages above +1 V and below -2.0 V that appear as broad peaks in the dI/dV spectrum. These voltage values are in rough agreement with the molecular states observed in STM, and also electronic transitions in the theoretical literature¹⁸, but the peaks appear significantly broadened and a direct comparison is obscured by the relatively large direct tunneling background in the TJ device. Confirming these resonances result from VOPc molecular states, control measurements of a sample without VOPc showed only direct tunneling without any indication of resonance peaks.

To mimic the spatially averaged nature of the TJ devices, STS data were collected at different sites within the VOPc molecule and at different positions across the layer. These 21 tunneling spectra were then normalized to their maximum dI/dV signal and averaged together to generate the wine-colored curve in Fig. 4. This process results in broadened peaks around -2V and + 1.5 V. To facilitate direct comparison, the direct tunneling contribution to Fig. 3e was removed by fitting the curve to the Fowler-Nordheim model and subtracting it from the dI/dV response of the VOPc-TJ device (green curve, Fig. 4). In this model, the direct tunneling current is given by (see Supplementary Note S5)⁴⁹:

$$I_b = f_0 \frac{4 \pi m_{eff} q}{f_1 h^3} \int_0^{\mu} E^{\frac{1}{2}} (f_1 - E)^{\frac{1}{2}} (\mu - E) e^{-\frac{4 \kappa f_2 (f_1 - E)^{\frac{3}{2}}}{3F}} dE \quad (1)$$

The result of this fitting process for the VOPc device is shown as a black dashed line in Fig. 3e, yielding $f_1 = 9.41$ eV and $f_2 = 0.15$ for both positive and negative voltage. However, different parameters optimize the positive and negative voltage regions for f_0 (sample area), $f_0 = 1.6 \times 10^{-13}$ and $f_0 = 2.6 \times 10^{-13}$, respectively. The results of a similar analysis performed on

the hBN devices discussed in Fig. 2a are shown in Extended Data Fig. 5. The difference between this calculated direct-tunneling background and the experimental data is shown in Fig. 4 (green curve). This residue highlights the major resonant tunneling features in the spectra, which can themselves be modeled using the following Gaussian function $\Gamma(E)$ for each resonance, with a defect current given by¹⁴ (see Supplementary Note S5)

$$I_d = \int_{-\infty}^{\infty} (f(E) - f(E - F)) \Gamma(E) dE \quad (2)$$

This analysis yields three resonances centered at voltages of +1.6 V, -1.1 V, and -2.05 V (Fig. 4, black dashed curve).

Comparing the averaged STS data (wine-colored curve) with the background-subtracted tunnel junction response (green curve) reveals excellent agreement in both the gap (1.63 V) and the width of the heterogeneously broadened ensembles. This result strongly supports the hypothesis that the tunneling spectra from the tunnel junction represent a spatial average over the VOPc bilayer, with the peak width dominated by real variations in tunneling current as a function of position within the VOPc molecule and for different local configurations of the bilayer.

In summary, we have demonstrated the encapsulation of quantum point defects and molecules within a tunnel junction constructed from 2D materials, establishing a versatile and modular technique that can be applied to a wide variety of quasi-0D quantum systems. The device structure protects the QPDs and molecules during the fabrication processes, prevents direct contact between metal contacts and the 0D quantum systems (pinholes), and enables a highly sensitive readout of the electronic states of the intrinsic defects and molecular states. We have demonstrated tunneling spectroscopy of carbon-related defects within a MLG/C-doped hBN/MLG tunnel junction device and VOPc molecular qubits encapsulated within a similar device structure

(MLG/hBN/VOPc/hBN/MLG). Tunneling spectroscopy of the former shows atomic-like resonance states of the intrinsic carbon-related defects in hBN, while the latter reveals broad resonance peaks in the VOPc films that are quantitatively consistent with STS of HOPG/hBN/VOPc half-devices and theory predictions of electronic structure¹⁸. The relative ease of fabrication and protective encapsulation demonstrates a facile approach to electronic tunneling spectroscopy for small ensembles of quasi-0D quantum systems that should be of interest for a wide variety of molecular and solid-state systems. Further, when combined with the extensive literature demonstrating high-fidelity quantum readout of electronic and nuclear spin states in related solid-state systems^{16,29,30,50}, this work provides a clear path to a dramatic expansion in the phase space of potential quantum systems to include optically inert but electrically active QPDs, molecules, and adatoms and their straightforward integration with existing solid-state quantum technologies.

References

1. Gottscholl, A. *et al.* Initialization and read-out of intrinsic spin defects in a van der Waals crystal at room temperature. *Nat Mater* **19**, 540–545 (2020).
2. Wolfowicz, G. *et al.* Quantum guidelines for solid-state spin defects. *Nature Reviews Materials* **6**, 906–925 (2021).
3. Zhang, G., Cheng, Y., Chou, J. P. & Gali, A. Material platforms for defect qubits and single-photon emitters. *Applied Physics Reviews* **7**, (2020).
4. Zhong, T. & Goldner, P. Emerging rare-earth doped material platforms for quantum nanophotonics. *Nanophotonics* **8**, 2003–2015 (2019).
5. Ortú, A., Holzapfel, A., Etesse, J. & Afzelius, M. Storage of photonic time-bin qubits for up to 20 ms in a rare-earth doped crystal. *npj Quantum Inf* **8**, (2022).
6. Gaita-Ariño, A., Luis, F., Hill, S. & Coronado, E. Molecular spins for quantum computation. *Nature Chemistry* **11**, 301–309 (2019).
7. Yu, C. J., Von Kugelgen, S., Laorenza, D. W. & Freedman, D. E. A Molecular Approach to Quantum Sensing. *ACS Cent Sci* **7**, 712–723 (2021).
8. Atzori, M. *et al.* Room-Temperature Quantum Coherence and Rabi Oscillations in Vanadyl Phthalocyanine: Toward Multifunctional Molecular Spin Qubits. *J Am Chem Soc* **138**, 2154–2157 (2016).

9. Stern, H. L. *et al.* A quantum coherent spin in hexagonal boron nitride at ambient conditions. *Nat Mater* (2024).
10. Atzori, M. & Sessoli, R. The Second Quantum Revolution: Role and Challenges of Molecular Chemistry. *Journal of the American Chemical Society* **141**, 11339–11352 t (2019).
11. Zadrozny, J. M., Niklas, J., Poluektov, O. G. & Freedman, D. E. Millisecond coherence time in a tunable molecular electronic spin qubit. *ACS Cent Sci* **1**, 488–492 (2015).
12. Becher, C. *et al.* 2023 roadmap for materials for quantum technologies. *Materials for Quantum Technology* **3**, (2023).
13. Chandni, U., Watanabe, K., Taniguchi, T. & Eisenstein, J. P. Signatures of Phonon and Defect-Assisted Tunneling in Planar Metal-Hexagonal Boron Nitride-Graphene Junctions. *Nano Lett* **16**, 7982–7987 (2016).
14. Greenaway, M. T. *et al.* Tunnel spectroscopy of localised electronic states in hexagonal boron nitride. *Commun Phys* **1**, (2018).
15. Grzeszczyk, M. *et al.* Electrical excitation of carbon centers in hexagonal boron nitride with tuneable quantum efficiency. (2023).
16. Anders, M. A., Lenahan, P. M., Harmon, N. J. & Flatté, M. E. A technique to measure spin-dependent trapping events at the metal-oxide-semiconductor field-effect transistor interface: Near zero field spin-dependent charge pumping. *J Appl Phys* **128**, (2020).
17. Frantz, E. B. *et al.* Effects of 29Si and 1H on the near-zero field magnetoresistance response of Si/SiO₂interface states: Implications for oxide tunneling currents. *Appl Phys Lett* **119**, (2021).
18. Mattioli, G., Filippone, F. & Bonapasta, A. A. Controlling the magnetic properties of a single phthalocyanine molecule through its strong coupling with the GaAs surface. *Journal of Physical Chemistry Letters* **1**, 2757–2762 (2010).
19. Spruijtenburg, P. C., Amitonov, S. V., Wiel, W. G. V. Der & Zwanenburg, F. A. A fabrication guide for planar silicon quantum dot heterostructures. *Nanotechnology* **29**, (2018).
20. Verjauw, J. *et al.* Path toward manufacturable superconducting qubits with relaxation times exceeding 0.1 ms. *npj Quantum Inf* **8**, (2022).
21. Moxim, S. J. *et al.* Observation of Radiation-Induced Leakage Current Defects in MOS Oxides with Multifrequency Electrically Detected Magnetic Resonance and Near-Zero-Field Magnetoresistance. *IEEE Trans Nucl Sci* **67**, 228–233 (2020).
22. Stegner, A. R. *et al.* Electrical detection of coherent 31P spin quantum states. *Nat Phys* **2**, 835–838 (2006).
23. Malissa, H. *et al.* Room-temperature coupling between electrical current and nuclear spins in OLEDs. *Science (1979)* **345**, 1487–1490 (2014).
24. Petta, J. R. *et al.* *Coherent Manipulation of Coupled Electron Spins in Semiconductor Quantum Dots*. (2024).
25. Koppens, F. H. L. *et al.* Driven coherent oscillations of a single electron spin in a quantum dot. *Nature* **442**, 766–771 (2006).

26. Harmon, N. J., Ashton, J. P., Lenahan, P. M. & Flatté, M. E. Spin-dependent capture mechanism for magnetic field effects on interface recombination current in semiconductor devices. *Appl Phys Lett* **123**, (2023).

27. Weng, Z., Gillin, W. P. & Kreouzis, T. Modelling and fitting the Polaron Pair Magnetoconductance model to obtain a realistic local hyperfine field in Tris-(8-hydroxyquinoline)aluminium based diodes. *Sci Rep* **9**, (2019).

28. Joshi, G. *et al.* High-Field Magnetoresistance of Organic Semiconductors. *Phys Rev Appl* **10**, (2018).

29. Ryan, J. T., Lenahan, P. M., Krishnan, A. T. & Krishnan, S. Spin dependent tunneling spectroscopy in 1.2 nm dielectrics. *J Appl Phys* **108**, (2010).

30. Gilbert, W. *et al.* On-demand electrical control of spin qubits. *Nat Nanotechnol* **18**, 131–136 (2023).

31. Abhyankar, N. *et al.* Recent advances in microresonators and supporting instrumentation for electron paramagnetic resonance spectroscopy. *Review of Scientific Instruments* **93**, (2022).

32. Wang, C. *et al.* Towards practical quantum computers: transmon qubit with a lifetime approaching 0.5 milliseconds. *npj Quantum Inf* **8**, (2022).

33. Zomer, P. J., Guimarães, M. H. D., Brant, J. C., Tombros, N. & Van Wees, B. J. Fast pick up technique for high quality heterostructures of bilayer graphene and hexagonal boron nitride. *Appl Phys Lett* **105**, (2014).

34. Klein, D. R. *et al.* Enhancement of interlayer exchange in an ultrathin two-dimensional magnet. *Nature Physics* **15**, 1255–1260 (2019).

35. Iwasaki, T. *et al.* Bubble-Free Transfer Technique for High-Quality Graphene/Hexagonal Boron Nitride van der Waals Heterostructures. *ACS Appl Mater Interfaces* **12**, 8533–8538 (2020).

36. Dean, C. R. *et al.* Boron nitride substrates for high-quality graphene electronics. *Nat Nanotechnol* **5**, 722–726 (2010).

37. Liu, W. *et al.* Spin-active defects in hexagonal boron nitride. *Materials for Quantum Technology* **2**, (2022).

38. Weston, L., Wickramaratne, D., Mackoit, M., Alkauskas, A. & Van De Walle, C. G. Native point defects and impurities in hexagonal boron nitride. *Phys Rev B* **97**, (2018).

39. Strand, J., Larcher, L. & Shluger, A. L. Properties of intrinsic point defects and dimers in hexagonal boron nitride. *Journal of Physics Condensed Matter* **32**, (2020).

40. Azevedo, S., Kaschny, J. R., De Castilho, C. M. C. & Mota, F. D. B. Erratum: Theoretical investigation of native defects in a boron nitride monolayer (Nanotechnology (2007)18 (495707)). *Nanotechnology* **23**, (2012).

41. Bonizzoni, C. *et al.* Coherent coupling between Vanadyl Phthalocyanine spin ensemble and microwave photons: Towards integration of molecular spin qubits into quantum circuits. *Sci Rep* **7**, (2017).

42. Cimatti, I. *et al.* Vanadyl phthalocyanines on graphene/SiC(0001): Toward a hybrid architecture for molecular spin qubits. *Nanoscale Horiz* **4**, 1202–1210 (2019).

43. Melville, O. A., Lessard, B. H. & Bender, T. P. Phthalocyanine-Based Organic Thin-Film Transistors: A Review of Recent Advances. *ACS Appl Mater Interfaces* **7**, 13105–13118 (2015).
44. Tomoda, H., Saito, S. & Shiraishi+, S. *The Chemical Society of Japan 1983 SYNTHESIS OF METALLOPHTHALOCYANINES FROM PHTHALONITRILE WITH STRONG ORGANIC BASES. CHEMISTRY LETTERS* (1983).
45. Wang, P. *et al.* Scalable Synthesis of Monolayer Hexagonal Boron Nitride on Graphene with Giant Bandgap Renormalization. *Advanced Materials* **34**, (2022).
46. Rochford, L. A., Hancox, I. & Jones, T. S. Understanding domain symmetry in vanadium oxide phthalocyanine monolayers on Au (111). *Surf Sci* **628**, 62–65 (2014).
47. Koll, W. *et al.* Formation of Oriented Bilayer Motif: Vanadyl Phthalocyanine on Ag(100). *The Journal of Physical Chemistry C* (2024).
48. Zhang, Y. *et al.* Electronic structure of the organic semiconductor vanadyl phthalocyanine (VO-Pc). *J Mater Chem* **17**, 1276–1283 (2007).
49. Fowler, R. H. & Nordheim, L. *Electron Emission in Intense Electric Fields. Source: Proceedings of the Royal Society of London. Series A, Containing Papers of a Mathematical and Physical Character* **119**, (1928).
50. Bonizzoni, C., Ghirri, A., Santanni, F. & Affronte, M. Quantum sensing of magnetic fields with molecular spins. *npj Quantum Inf* **10**, (2024).

Acknowledgments We acknowledge financial support from the National Science Foundation (NSF) QII-TAQS under award numbers OMA-1936219 and MPS-1936219, NSF NRT-QISE DGE-2244045, as well as the Asian Office of Aerospace Research and Development (AOARD) under award number FA238620-1-4052. Partial funding for shared facilities used in this research was provided by the Center for Emergent Materials: an NSF MRSEC under award number DMR-2011876. Work done at Ames National Laboratory was supported by the U.S. Department of Energy, Office of Basic Energy Science, Division of Materials Sciences and Engineering. Ames National Laboratory is operated for the U.S. Department of Energy by Iowa State University under Contract No. DE-AC02-07CH11358. We also thank Ronald Kawakami in the Department of Physics at The Ohio State University for providing access to the transfer microscope setup in his lab, Anthony Harbo Torres in the Department of Physics at The Ohio State University for AFM

analysis, Yuxin Zhang and Chun Ning Lau in the Department of Physics at The Ohio State University for providing the exfoliated MANA hBN, Zetian Mi in the Department of Electrical Engineering and Computer Science at the University of Michigan for providing hBN for STM measurements, Chhatra Tamang Lama and Yueguang Shi in the Department of Physics and Astronomy at the University of Iowa for theoretical calculations, and Joshua Kennedy at Air Force Research Laboratory (AFRL) for fruitful discussion and providing facilities for electron beam lithography.

Authur contributions E. J.H. conceived the experiments and supervised the project. Z. P., M. H., M. K., E. P. H., and D. P. stacked or fabricated the 2D-TJ devices. D. E. F. and R. G. selected and produced the VOPc. Under the supervision of J. G., W. K. deposited the VOPc and with the assistance of F. A. performed the STM and STS measurements. M. K. with assistance of Z. P., M. H., and E. P. H performed the tunneling measurements of the 2D-TJ devices. M. K. analyzed the data with the assistance of W. K. in analyzing the STM data. Under the supervision of M. F., M. M. S. developed theoretical calculations for modeling direct tunneling and resonant tunneling. Under supervision of P. C., M. X. synthesized the Ames hBN. T. T. provided the MANA hBN. All authors contributed to the writing of the manuscript.

Competing interest The authors declare no competing interests.

Supplementary Information is available for this paper.

Correspondence and requests for materials should be addressed to Ezekiel Johnston-Halperin.

Figures

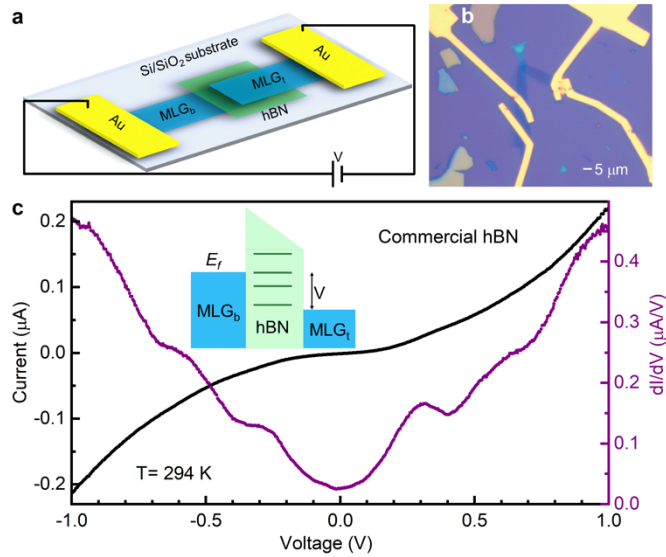


Fig. 1| Electrical characterization of a hBN tunnel junction (hBN-TJ) device. **a**, Schematic of the hBN-TJ device structure. The 2D heterostructure features multi-layer graphene (MLG) contacts to a hBN barrier layer. **b**, Optical image of a hBN-TJ device. **c**, I-V, black curve, and dI/dV, purple curve, at room temperature. Plateaus in I-V and broad peaks in dI/dV are due to the resonant tunneling caused by native defect states in the hBN barrier. Inset, a schematic of the energy diagram of the TJ device. Discrete lines represent the energy states of the native defects within the hBN bandgap.

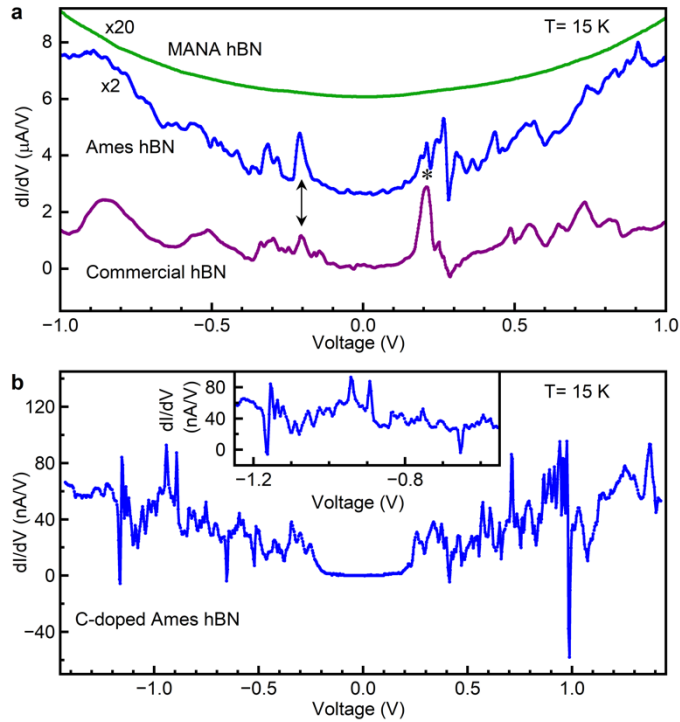


Fig. 2| Tunneling spectroscopy of quantum point defects in hBN. **a**, dI/dV of the hBN tunnel junction (hBN-TJ) devices at 15 K for three sources of pure hBN: commercial hBN from HQ Graphene, Ames hBN, and MANA hBN. Tunneling spectrum of the MANA hBN device reveals no significant resonant tunneling peaks (See Extended Data Fig. 2). **b**, dI/dV of carbon-related defects in Ames hBN at 15 K. Inset, a zoomed in dI/dV around -1 V, indicating the sharpness of the atomic-like resonant peaks.

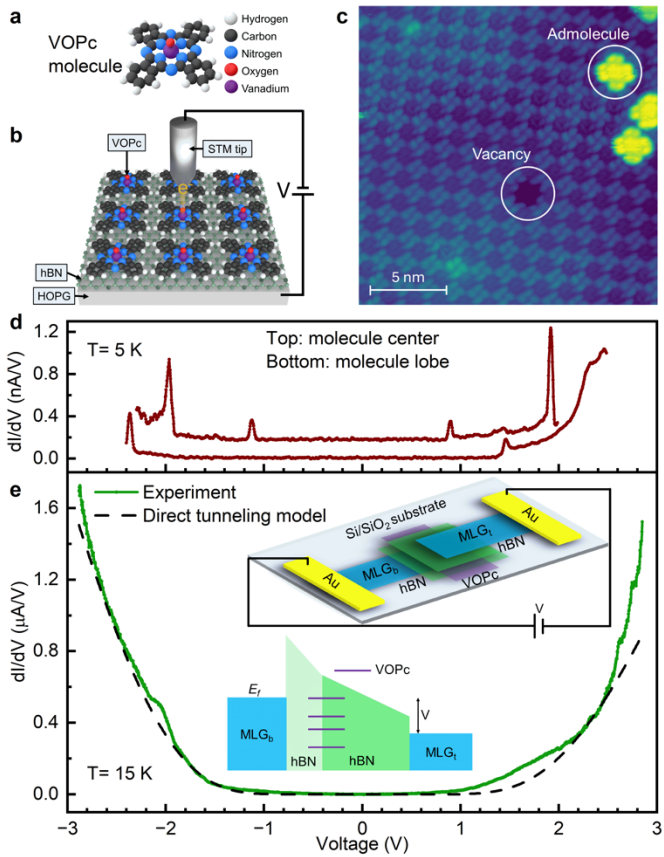


Fig. 3| STM of molecular qubits: VOPc on hBN **a**, Structure of VOPc molecule. **b**, A schematic of the STM setup containing a ‘half tunnel junction’ device as studied by STM and STS **c**, STM topographic image of a bilayer of VOPc deposited on a monolayer hBN on an HOPG substrate (STM imaging conditions: +2.3 V, 326 pA). **d**, dI/dV of VOPc at 5 K measured by an STM setup with tip located at the molecule center (top curve) or molecule lobe (bottom curve). **e**, dI/dV of VOPc encapsulated in 2D-TJ device at 15 K (green curve). The dashed black curve is direct tunneling model. Top inset, a schematic of the VOPc-TJ device with heterostructure of MLG/hBN/VOPc/hBN/MLG. Bottom inset, a schematic of the energy diagram of the device with discrete lines representing molecular states of VOPc.

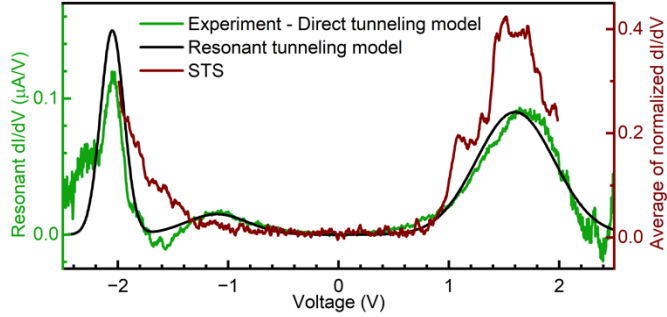
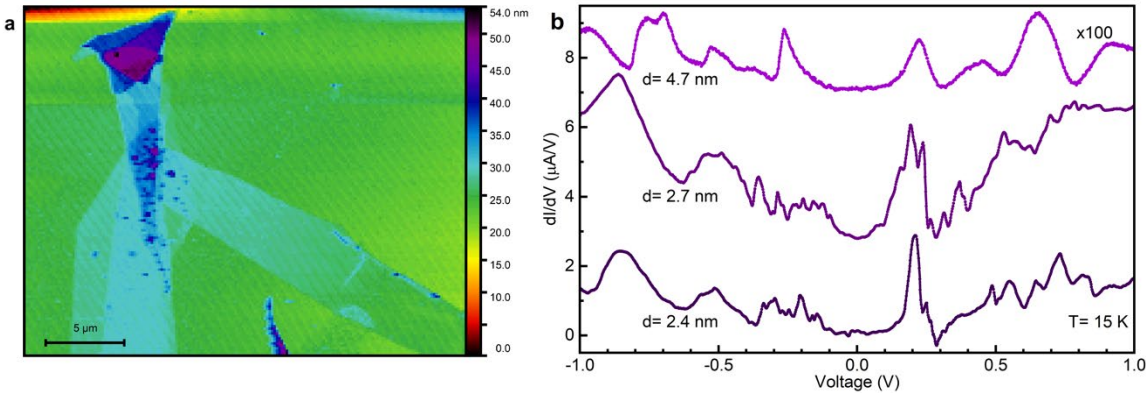
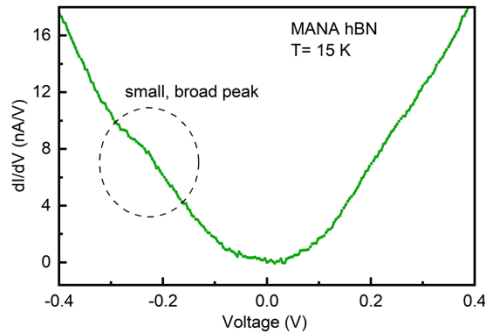


Fig. 4| Comparison between spatially-averaged STS and VOPc devices. The green curve shows the experimental dI/dV (green curve in Fig. 3e) subtracted from direct tunneling model for a VOPc-TJ device (i.e., black curve in Fig. 3e). The black curve is the calculated resonant dI/dV , and the wine curve represent the average of dI/dV scans as measured by STS on a VOPc bilayer film on hBN. STS were taken at 21 different tip locations and were normalized before averaging.

Extended Data

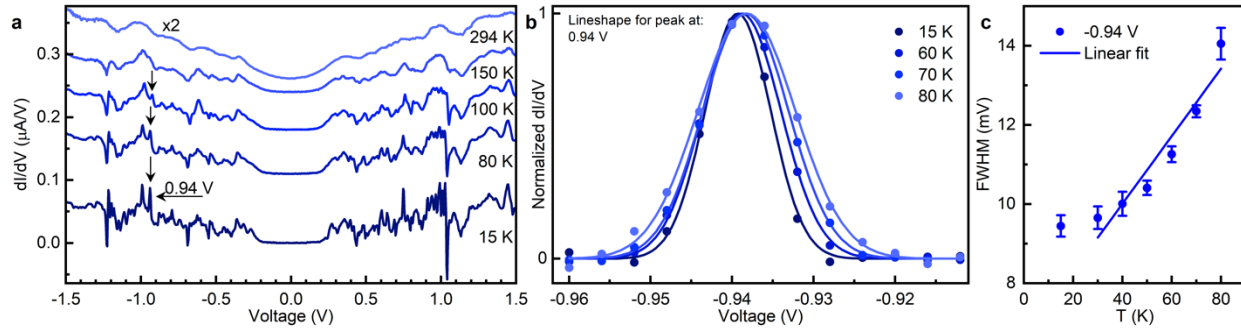


Extended Data Fig. 1| AFM image and the dependency of tunneling spectroscopy on hBN thickness. **a**, An AFM scan image of the three-layer stack (MLG/hBN/MLG) for the device, with the corresponding optical image shown in Fig. 1b. **b**, dI/dV measurements for three hBN-TJ devices with various commercial hBN flack thicknesses: 2.4, 2.7 and 4.7 nm. The data reveal that increasing the hBN thickness led to a decrease in direct tunneling and resonance peaks become broader with less sharp resonance features.



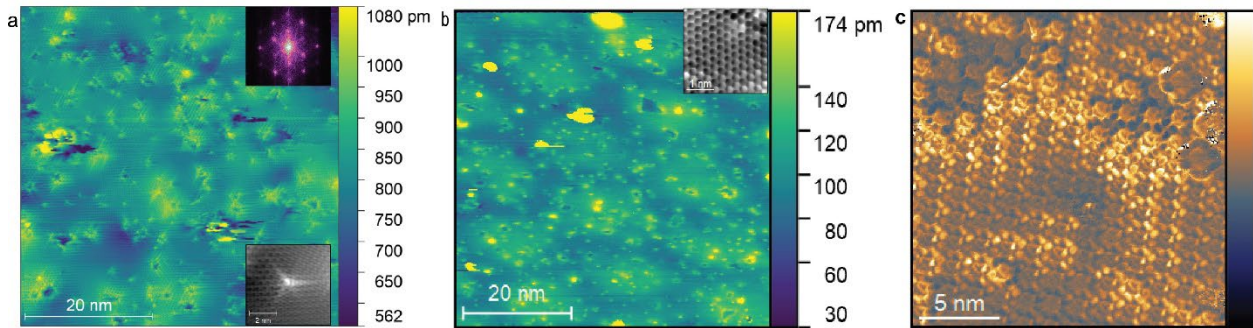
Extended Data Fig. 2| Significant suppression of resonance tunneling in MANA hBN.

Zooming in on the dI/dV data in Fig. 2a (green curve) shows only a small and broad resonant tunneling peak around -0.25 V for the MANA hBN-TJ device.

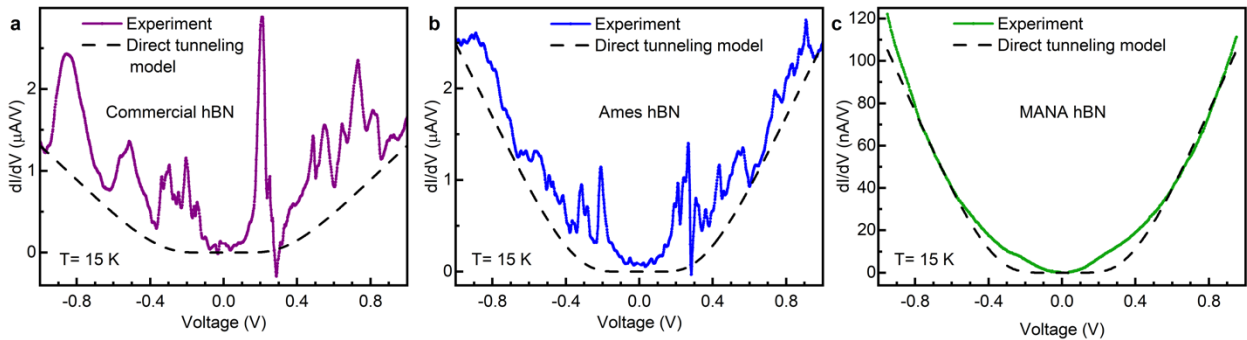


Extended Data Fig. 3|Temperature dependency of tunneling spectroscopy for a C-doped hBN tunnel junction device. a, dI/dV spectra at various temperatures: 15 K, 80 K, 100 K, 150 K, and 290 K. The data reveals that the resonant tunneling becomes broader as the temperature increases, and above 80 K, the line-shapes become distorted. **b,** Line-shape analysis of the sharp resonant peak at -0.94 V. The line-shapes are fitted with linear (to remove the baseline) and Lorentzian functions and normalized by its maximum for temperatures ranging from 15 K up to 80 K. The blue lines are the fit results. **c,** The full width at half maximum (FWHM) of the line-shape fitted results as a function of the temperature. The blue line is a linear fit to the data, indicating the line-

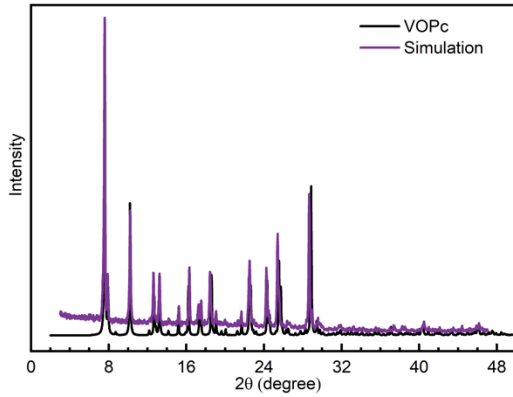
shape increases linearly by increasing the temperature up to 80 K. Above 80 K, the line-shapes are distorted and cannot be fitted.



Extended Data Fig. 4 | Sources of spatial variation in tunneling spectroscopy of VOPc on a hBN/HOPG half device. **a**, STM wide-area topographic image of a bare monolayer hBN on HOPG with atomic resolution and defects. Top inset, 2D-FFT of image, bottom inset, close-up of a single-point defect. **b**, Another STM topographic image of a bare monolayer hBN on HOPG. There is a moire pattern (period ~ 14 nm) due to the lattice mismatch of the hBN and the HOPG. Inset, hBN atomic resolution. **c**, Constant-current dI/dV map of VOPc bilayer on hBN/HOPG acquired simultaneously with topographic image in Fig. 3c. Long distance fluctuations in contrast may reflect defects or the moire lattice in the underlying hBN. STM imaging conditions: **a**, (+2.6V, 78pA); **b**, (+2.37V, 20pA) **inset**, (+620mV, 190pA); and **c**, (+2.3V, 326pA).



Extended Data Fig. 5| Direct tunneling model. dashed curves are calculated direct tunneling at $T = 15$ K for various hBN-TJ device: **a**, commercial hBN, **b**, Ames hBN, and **c**, MANA hBN.



Extended Data Fig. 6| powder X-ray diffraction (PXRD) patterns for VOPc, simulated (black) vs. experimental (purple) Data were collected at room temperature using CuK α 1 radiation ($\lambda = 1.5406$ Å). Simulation of PXRD pattern was based on single crystal X-ray diffraction data of VOPc as reported in Reference 2.

Supplementary information

Supplementary Note S1: stacking and fabrication of hBN tunnel junction (hBN-TJ) devices

After exfoliation of graphite on the Si/SiO₂ substrate, we identify the top and bottom MLG flakes with appropriate thickness and shapes using an optical microscope. To create a stack of the heterostructure with 2D materials, we initiate the process by transferring the top MLG. This is

accomplished by picking it up using a polycarbonate (PC) film coated on a polydimethylsiloxane (PDMS) stamp and a glass slide at a temperature of 90°C. Subsequently, hBN is transferred onto the top MLG flake, also picked up at a temperature of 90°C. This procedure ensures that the interfaces of the hBN layer remain clean, with no direct contact with solvents or polymers. In the final step, the top MLG/hBN layers are delicately placed onto the bottom MLG, previously exfoliated on a Si/SiO₂ substrate, at a temperature of 105°C. The entire stack is then heated to 150°C for about 10 minutes for the adhesion of the 2D heterostructure onto the substrate. After allowing the stack to cool, we dissolve the polycarbonate (PC) film by immersing the stack in chloroform for approximately 4 minutes, adjusting the duration based on the amount of PC film present on the substrate. The subsequent step involves annealing the sample for a duration of 90 minutes at a temperature of 350°C under vacuum conditions. Specifically, we employ a gradual thermal ramp-up and ramp-down, with a 90-minute rise from room temperature to 350°C, 90 minutes of annealing at 350°C, followed by a 90-minute descent to room temperature to prevent thermal shock. This process eliminates any residues of polymers and solvents from the stack while enhancing the interfacial bonding between the layers of the stack. We employ electron beam lithography to pattern gold contacts for establishing electrical connections. Following the spin coating of MMA and PMMA (both deposited at 3000 RPM for 45 seconds), we use electron beam to write the contact patterns. The pattern is then developed with a mixture of MIBK/IPA for approximately 70 seconds, adjusting the duration based on the amount of resist residue on the sample. Finally, a 5 nm Chromium (Cr) film is deposited, followed by a 150 nm layer of gold (Au) for the metal contacts. We utilize acetone for the lift-off process of the gold. At the end the sample is wire-bonded on a chip carrier for transport measurements.

Supplementary Note S2: Ames hBN synthesis

Synthesis of hBN takes place in a high-pressure furnace at 3.2 GPa, in a process that co-synthesizes both hBN and MgB₂. The temperature is increased to 1380 °C before slowly cooling down to 650 °C. The flux ratio of Mg:B elements in a BN crucible is 1:0.7. The synthesis process for carbon doped hBN is similar to that described above with the exception that 2% of the B is replaced by C, resulting in a flux ratio of Mg: B: C of 1: 0.686: 0.014.

Supplementary Note S3: VOPc synthesis and characterization

General Considerations: Vanadyl(IV) sulfate pentahydrate was purchased from Alfa Aesar, 1-pentanol and phthalonitrile were purchased from Sigma-Aldrich, and diazabicyclo[5.4.0]undec-7-ene (DBU) was purchased from Chem-Impex International. All chemicals were used as received.

Synthesis: Vanadyl(IV) phthalocyanine (VOPc) was prepared according to an adapted literature procedure¹. A 250 mL round-bottom flask was charged with vanadyl(IV) sulfate pentahydrate (0.7604 g, 3 mmol, 1.2 eq.), phthalonitrile (1.2817 g, 10 mmol, 4 eq.), DBU (1.5 mL, 10 mmol, 4 eq.), 40 mL 1-pentanol, and a stir bar. The flask was then refluxed at 145 °C for 16 hours. The dark blue-purple product was isolated via vacuum filtration, rinsed with 100 mL deionized water, 100 mL ethanol, and 500 mL ethyl acetate, and dried for 20 minutes. Product yield was 0.2998 g (20.7%). MALDI-TOF mass spectrometry (m/z): [M]⁺ calculated for C₃₂H₁₆N₈VO, 579.089, 580.092, 581.095, 580.086; found 578.859, 579.037, 579.140, 579.919. FTIR (cm⁻¹): 436.9, 504.9, 567.8, 637.9, 723.4, 750.2, 774.9, 800.7, 836.8, 872.8, 896.5, 958.4, 998.5, 1072.7, 1117.1, 1156.2, 1285.0, 1330.4, 1413.8, 1460.2, 1496.3, 1606.5, 3668.5, 3744.8, 3848.9.

Powder X-Ray Diffraction: Bulk purity was evaluated through powder X-ray diffraction (PXRD) (Extended Data Fig. 6). A powdery sample of VOPc was loaded into a PXRD mask between pieces of Kapton tape and PXRD patterns were collected on a STOE STADI MP diffractometer equipped with CuK α 1 radiation ($\lambda = 1.5406 \text{ \AA}$) located at the Integrated Molecular Structure Education and

Research Center of Northwestern University. Simulation of PXRD pattern was produced from crystallographic data previously collected².

Other Physical Measurements: MALDI-TOF mass spectrometry (MS) measurements were collected on a Bruker RapiFlex Tissue Typer mass spectrometer located at the Integrated Molecular Structure Education and Research Center of Northwestern University. No matrix was necessary for the ablation and desorption of VOPc in MALDI-TOF MS measurements. Infrared spectra were recorded on a Bruker Alpha II Compact FTIR spectrometer equipped with an attenuated total reflectance accessory located at the Department of Chemistry Instrumentation Facility of Massachusetts Institute of Technology.

Supplementary Note S4: stacking and fabrication of VOPc tunnel junction (VOPc-TJ) device
Heterostructures were assembled in a five-layer stack using a modification of the process described for MLG/hBN/MLG structures above: an initial layer of MANA hBN with target thickness of 1.5 nm was stacked onto a bottom MLG electrode, and then the polycarbonate film was removed using chloroform. This structure was transferred into the STM chamber for deposition of VOPc using an identical protocol to the one reported for STM studies above. The stack, now with VOPc as the top layer, was then removed from the STM chamber and a second MANA hBN layer (target thickness of 3.5 nm) and the top MLG electrode were placed on top with an alignment that prevents shorting of the two MLG layers, resulting in a stack structure of MLG/hBN(1.5 nm)/VOPc bilayer/hBN (3.5 nm)/MLG (see inset to Fig. 3e).

Supplementary Note S5: direct tunneling and resonant tunneling models

In the direct tunneling model (Equation 1 in the main text), I_b is resonant tunneling current, m_{eff} is the effective mass of electron in hBN³, $0.588 m_o$, where m_o is mass of free electron, q is charge of electron, h is Planck constant, E is energy, and $\mu = 3.77$ eV is chemical potential of graphene⁴,

and κ is $\pi\sqrt{8m_{eff}/h}$. f_0 , f_1 , and f_2 are three free parameters. The parameter f_0 rescales the current to match the effective area of the sample, and f_1 is the effective height of the barrier which is generally the sum of the chemical potential and thermionic work function. The parameter f_2 modifies the applied electric field, to an effective F for this model.

In the resonant tunneling model (Equation 2 in the main text), I_d is resonant tunneling current, $f(E)$ is Fermi-Dirac distribution, and Gaussian function for each resonance is

$$\Gamma(E) = d_0 e^{-(\frac{E-d_1}{d_2})^2} \quad (S1)$$

where, d_0 , d_1 , and d_2 are the conductance peak height, voltage of the peak, and linewidth, respectively.

Supplementary Information References

1. Tomoda, H.; Saito, S.; Shiraishi, S. Synthesis of Metallophthalocyanines from Phthalonitrile with Strong Organic Bases. *Chem. Lett.* **12**, 313–316 (1983).
2. Ramadan, A. J.; Rochford, L. A.; Keeble, D. S.; Sullivan, P.; Ryan, M. P.; Jones, T. S.; Heutz, S. Exploring High Temperature Templating in Non-Planar Phthalocyanine/Copper Iodide (111) *Bilayers. J. Mater. Chem. C* **3**, 461–465 (2014).
3. Y. Malozovsky et al., Accurate Ground State Electronic and Related Properties of Hexagonal Boron Nitride (h-BN), *Journal of Modern Physics* 11, no. 6 (2020).
4. Jannatul Mawwa et al., In-Plane Graphene/Boron Nitride Heterostructures and Their Potential Application as Toxic Gas Sensors, *RSC Advances* 11, no. 52 (2021).

Data availability

The data that support the plots within this paper and other finding of this study are available from the corresponding author upon reasonable request.